PROCEEDINGS OF SPIE

SPIEDigitalLibrary.org/conference-proceedings-of-spie

Challenges for optical turbulence characterization and prediction at optical communication sites

Florian Quatresooz, Gilles Orban de Xivry, Olivier Absil, Danielle Vanhoenacker-Janvier, Claude Oestges

Florian Quatresooz, Gilles Orban de Xivry, Olivier Absil, Danielle Vanhoenacker-Janvier, Claude Oestges, "Challenges for optical turbulence characterization and prediction at optical communication sites," Proc. SPIE 12777, International Conference on Space Optics — ICSO 2022, 127775O (12 July 2023); doi: 10.1117/12.2691034

SPIE.

Event: International Conference on Space Optics — ICSO 2022, 2022, Dubrovnik, Croatia

International Conference on Space Optics—ICSO 2022

Dubrovnik, Croatia

3–7 October 2022

Edited by Kyriaki Minoglou, Nikos Karafolas, and Bruno Cugny,

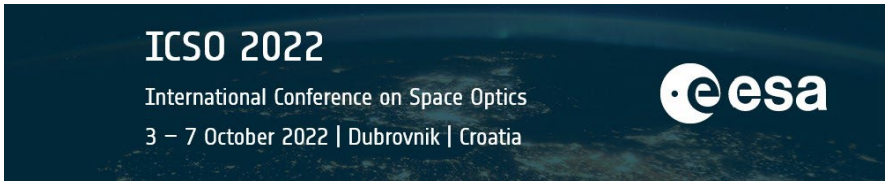

Challenges for optical turbulence characterization and prediction at optical communication sites

International Conference on Space Optics — ICSO 2022, edited by Kyriaki Minoglou, Nikos Karafolas, Bruno Cugny, Proc. of SPIE Vol. 12777, 127775O · © 2023 ESA and CNES · 0277-786X · doi: 10.1117/12.2691034

Challenges for optical turbulence characterization and prediction at optical communication sites

Florian Quatresooz[a], Gilles Orban de Xivry[b], Olivier Absil[b], Danielle Vanhoenacker-Janvier[a], and Claude Oestges[a]

[a]ICTEAM Institute, Université catholique de Louvain (UCLouvain), Louvain-la-Neuve, Belgium
[b]Space sciences, Technologies, and Astrophysics Research (STAR) Institute, Université de Liège (ULiège), Liège, Belgium

ABSTRACT

Modelling of atmospheric optical turbulence has been of interest in astronomy for several decades, e.g. for site characterization and flexible scheduling. Nowadays, it is also considered for free-space optical communications, namely to conduct site selection and to design future optical communication systems. In this work, a general approach relying on numerical weather prediction simulations in order to perform optical turbulence prediction is presented. The approach makes use of the Weather Research and Forecasting model and raises several challenges. The latter, such as the choice of the C_n^2 models or the required temporal and spatial resolutions, are first discussed with regards to the literature. Then, optical turbulence prediction is conducted for the site of Redu, Belgium, illustrating the different challenges. These predictions are also compared with seeing measurements from a differential image motion monitor. The presented approach offers realistic seeing values that, however, do not follow rapid variations of the measured seeing. Origins of the discrepancies between measurements and predictions are to be found in the modelling of the boundary layer and motivate the use of a C_n^2 model relying on the turbulent kinetic energy. Further simulations and measurement campaigns at other optical communication sites are encouraged in order to refine some model parameters and compare statistically the prediction results.

Keywords: Free space optics, optical turbulence, Numerical Weather Prediction, atmospheric propagation

1. INTRODUCTION

The modelling of optical turbulence (OT) in the atmosphere is of particular interest for astronomers, optical and electrical engineers. Indeed, atmospheric turbulence perturbs optical waves propagating in the atmosphere independently of their origins, i.e. either coming from observed celestial objects or from optical communication satellites. Hence, similar challenges are faced.

Optical turbulence has been a major concern for ground-based optical astronomy since the nineteenth and twentieth centuries, when telescope apertures started to be sufficiently large such that the resolution was more limited by atmospheric turbulence than by diffraction.[1] The necessary theoretical and mathematical background about wave propagation in random medium has been progressively developed during the twentieth century,[2,3] and applied to optical astronomy.[4] Nowadays, atmospheric turbulence effects on optical waves are well understood and can be partially compensated thanks to adaptive optics.[5] However, accurate prediction of optical turbulence remains a challenge.

Commonly, atmospheric OT is described by the refractive index structure parameter C_n^2, which is a statistical quantity describing how strong the refractive index fluctuations are. It is often associated to Kolmogorov theory of turbulence[2] and varies with the geographic location (topography) and with time (diurnal and seasonal variations).[6] It is also varying with the altitude h, leading to $C_n^2(h)$ profiles. Models of C_n^2 profiles provide a complete statistical description of atmospheric turbulence effects on wave propagation. Based on their knowledge, other OT-related quantities can be derived, such as the seeing, the isoplanatic angle or the scintillation index.[4,7]

In order to obtain C_n^2 profiles, several approaches have been presented in the literature. Empirical models have been developed, such as the well-known Hufnagel-Valley model[7] for example. These models usually result from measurements of C_n^2 profiles, e.g. by making use of thermosondes. Other tools for C_n^2 profiling have

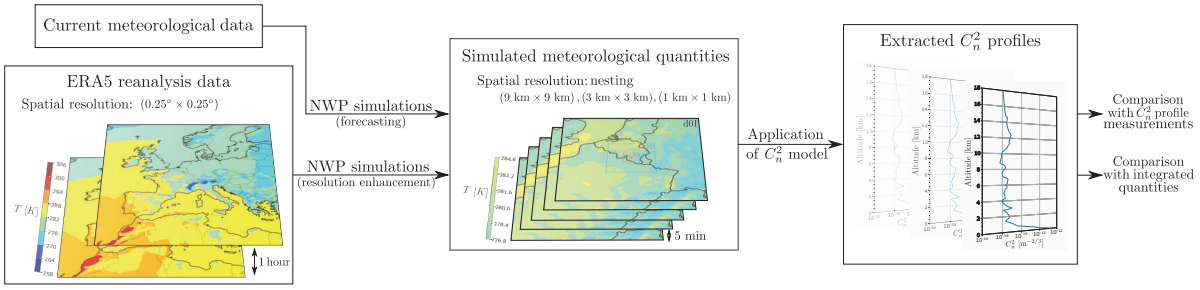

Figure 1: General approach to perform OT forecast based on NWP simulations.

also been developed and progressively installed at astronomical observatories.[8,9] Moreover, C_n^2 models relying on meteorological quantities have emerged, often based on Tatarskii's expressions.[2] Those are frequently used with meteorological quantities coming from radiosonde measurements, offering high-resolution vertical profiles.[10] However, a recent trend is to apply these models with meteorological quantities coming from numerical weather prediction (NWP) simulations instead.[11] This enables to substitute costly measurement campaigns and radiosonde launches by numerical simulations, as well as to perform OT forecast.

The idea of OT forecast for astronomy has already been presented in 1986: seeing forecasts, based on meteorological quantities, can be used to assist and optimize observation scheduling of telescopes.[12] Following this idea, the first numerical simulation of atmospheric turbulence for astronomical site selection was achieved in 1995.[13] Since then, many ground-based optical telescopes are equipped with tools monitoring OT quantities and with software performing real-time OT predictions based on NWP simulations.[14] It is now well accepted that OT forecast is paramount for optical astronomy, enabling flexible scheduling, site characterization and selection, instrument design and optimization.[15] Similarly, it will help for the design of optical communication systems and for site selection of future optical ground stations (OGS).[16] However, OT forecast is expected to be more challenging at those locations since, being located at lower altitudes than observatories, they suffer from increased turbulence.

In this paper, the general approach classically used to perform OT forecast with NWP simulations is firstly reminded (Sec. 2). The challenges arising from this approach are then discussed with regards to the literature in Sec. 3. This section also motivates the choices of parameters and models that have been made to perform OT forecast at Redu (Belgium), that is a potential location for optical ground stations in Belgium (see Sec. 4). Finally, seeing prediction are compared with measurements in Sec. 4. It highlights the limitations of NWP approaches to perform short-term seeing predictions at locations where OT in the boundary layer dominates. This is the first time OT is characterized at Redu.[17]

2. OPTICAL TURBULENCE FORECAST FROM NWP SIMULATIONS

The general approach proposed in this work is inspired from previous research on OT forecast for astronomical applications[14,15,18–20] and is presented in Fig. 1. Its purpose is to provide C_n^2 profiles above a given area and at a particular time based on meteorological quantities coming from NWP simulations. Depending on the origin of the meteorological data used to initialize NWP simulations, OT characterization or forecast can be achieved.

For OT characterization, i.e. the development of OT models and their comparison with measurements, reanalysis data are used as inputs to the NWP model. Those are meteorological quantities coming from large NWP simulations describing past atmospheric states that are stored in database, such as the ERA5 reanalysis data coming from ECMWF.[21] Since they have limited space ($0.25° \times 0.25°$) and time (1 hour) resolutions, NWP simulations are further used to obtain the meteorological quantities at the desired times and with the necessary spatial resolution. This is the first step depicted on the bottom left of Fig. 1. Alternatively, OT forecast is made possible by using current meteorological data and NWP simulations to achieve forecasting capabilities while ensuring the desired spatial and temporal resolutions.

In both cases, the NWP software applied in this work is the Weather Research and Forecasting (WRF) model developed by the National Center for Atmospheric Research (NCAR).[22] It enables to perform domain nesting, thus increasing the spatial resolution up to 1 km of grid spacing. The domain nesting is illustrated in the center of Fig. 1 where the three nested domains are visible. The example given is the ground temperature computed for Redu (Belgium) on February 14, 2019. The complete WRF parameterization is detailed in Sec. 3.1. At this stage, it is important to note that the main goal of using NWP simulations is to obtain 3D grids (latitude, longitude and altitude) of desired meteorological quantities at a given location. The spatial resolution of those grids can be chosen, as well as their temporal evolution, i.e. the time interval between each 3D grid (e.g. 5 minutes in Fig. 1).

Then, the next step is to use the simulated meteorological quantities to extract C_n^2 at all grid points, and especially above the location of interest. Hence, C_n^2 profiles are extracted, as well as their evolution in time. In order to obtain C_n^2 values based on meteorological quantities, a C_n^2 model is applied. Since several C_n^2 models have been developed in the literature, a choice of model must be made and is further explained in Sec. 3.2.

Finally, in the case of OT characterization, the obtained C_n^2 profiles can be compared and validated with measurements, as well as be used to compute (electromagnetic) quantities of interest. This includes for example the scintillation index, the seeing, and other quantities linked to C_n^2 profiles usually by means of analytical expressions. Therefore, depending on the availability of measurements, direct comparisons between measured and simulated C_n^2 profiles can be possible. Alternatively, if only measurements of integrated quantities of C_n^2 profiles are available, then the simulated C_n^2 profiles are firstly integrated accordingly and then compared with the measurements.

The approach presented in Fig. 1 is quite general and has been extensively used in the literature, not only to provide C_n^2 profiles but also to obtain C_n^2 ground values.[23,24] Nevertheless, its parameterization raises several challenges that are addressed in the next section.

3. PARAMETERIZATION AND ASSOCIATED CHALLENGES

Numerous parameters or models must be chosen to achieve accurate C_n^2 profile prediction. It leads to various choices related to the spatial and temporal resolutions, the C_n^2 model, the modelling of the boundary layer or the availability of measurements.

3.1 Spatial and temporal resolutions

Different kinds of NWP software for modelling the atmosphere are available, such as general circulation models (GCM), mesoscale models or large-eddy simulations (LES).[25] Each of them resolves atmospheric phenomena at different scales, offering their own spatial and temporal resolutions.

Since WRF belongs to the category of mesoscale models, it is applied to a limited area of Earth and can simulate mesoscale atmospheric phenomena ranging from kilometers to hundreds of kilometers. As mentioned previously, grid nesting is used to increase the spatial resolution near the location of interest, achieving horizontal resolution of 1 km.[20] This limitation is mostly computational and the resolution of the orographic data must also be considered when reducing further the grid spacing.

Vertically, the grid spacing is usually varying non-linearly, with smaller distance between levels close to ground and larger distance between levels at the top of the atmosphere. Close to ground, the spacing can be on the order of 10 meters, whereas, at high altitude, the spacing can be more than 500 m. In order to further reduce the vertical grid spacing, more levels should be added in the NWP software at the price of a larger computation time. In Ref. 20, it is suggested to use grid spacing of 100 meters or less to resolve OT.

Regarding the temporal resolution, it is intrinsically related to the time step required for avoiding numerical instabilities in NWP simulations (e.g. 1 to 5 seconds[20]). However, this is not the temporal resolution at which output meteorological data are recorded. Instead, they are saved every 5 minutes in this work.

Following these considerations, the configuration for WRF simulations at Redu is given in Tab. 1. The three nested domains are named d01, d02 and d03, with d01 being the largest but coarsest domain and d03 being the smallest but finest domain. In each domain, 250 vertical levels are used leading to an average vertical spacing

Table 1: Grid parameters from WRF simulations.

Domain	Grid resolution (km)	Number of grid points	Domain size (km)	Number of vertical levels	Vertical spacing between levels (m)
d01	9	79×79	711×711	250	∼80
d02	3	79×79	237×237	250	∼80
d03	1	79×79	79×79	250	∼80

between levels of approximately 80 meters, from the ground to 20 km of altitude. Levels are almost equally-distributed, with the largest level spacing being 100 meters and the smallest one being 60 meters. The top pressure of the atmosphere set for WRF simulations is 5000 Pa. For comparison with measurements, simulations start at least 6 hours prior to the time window where the measurements are available (6 hours of lead time).

The configuration of the WRF physical schemes used is: WSM6[26] for microphysics, Tiedtke[27] for cumulus physics, Dudhia[28] and RRTM[29] for shortwave and longwave radiations, and revised MM5[30] for the surface layer. For the planetary boundary layer physics, the MYNN 2.5[31] scheme is used as it solves for the turbulent kinetic energy (TKE) that can be added to WRF simulation outputs. This TKE is then used in the chosen C_n^2 model.

3.2 Choice of C_n^2 model

The choice of C_n^2 model is also a challenge. It corresponds to the step that enables to go from meteorological data to C_n^2 profiles useful to get OT-related quantities. The literature about optical C_n^2 models is rich and different models have been developed throughout the years. Several classifications of these models are possible:

- **Parametric vs. non-parametric models**: Non-parametric models provide expressions of the C_n^2 profile as a function of the altitude h only, i.e. $C_n^2(h)$. Such models have mostly been derived based on measurements and include the SLC daytime and nighttime models, the AFGL AMOS model, the CLEAR I model, etc.[32,33] On the contrary, parametric models rely on meteorological, temporal or geographical quantities, allowing to model spatial and temporal variations of the C_n^2 profiles. Their generic expression is $C_n^2(h, p, T, ...)$, with p the pressure and T the temperature, having variations in space and time. Models such as the Hufnagel-Valley model,[7] the HAP model[34] or the Dewan model[35] belong to this category for example.

  Parametric and non-parametric models have their own advantages and disadvantages: non-parametric models are simple to use but provide only mean profiles that are site-specific (i.e. based on the locations where the measurements have been taken), whereas parametric models need extra information and may involve more computation but give access to profiles based on local conditions.

- **Empirical vs. theoretical vs. numerical models**: Models can also be classified based on their origins. Empirical models come from measurements and are thus quite simple to use. However, they are site-specific and do not provide physical insights about optical turbulence. On the contrary, theoretical models, such as Tatarskii-based models,[2,32] rely on turbulence theory and involve different hypotheses. They offer better understanding of the modelled phenomena, even though they can involve some parameters that remain to be fixed, often based on measurements. They usually follow the generic expression:

$$C_n^2 = a^2 \alpha L_0^{4/3} M^2, \tag{1}$$

  where $a^2\alpha$ are constant parameters, L_0 is the outer scale of turbulence and $M = \frac{\partial n}{\partial z}$ is the refractive index vertical gradient. Models for L_0 and M are then required.

  Alternatively, a last category of models has recently emerged, grouping numerical models solving for the TKE in fluid mechanics simulations. They are of particular interest for OT forecast as meteorological data are often obtained thanks to NWP simulations. Hence, this latter can be adapted to compute and extract the TKE and then use it in a C_n^2 model.[18,20,36]

Furthermore, other classifications are also possible. For example, C_n^2 models can also be classified depending on the part of the atmosphere they describe (free atmosphere or surface layer), on the location they have been

designed for (e.g. for observatories at high altitude), on the time of the day (daytime or nighttime models), on the hypotheses used, as well as depending on their primary utility (for astronomical observations or for optical communications) and on the targeted wavelengths. Therefore, all of these factors must always be taken into account when using any C_n^2 model.

As a summary, the choice of C_n^2 model for OT forecast is not trivial. For OT characterization and prediction based on NWPs, chosen models are mostly *parametric* such that they depend on local meteorological quantities. This dependence can either be expressed through analytical expressions (*theoretical models*) or through expressions involving the TKE (*numerical models*). They usually describe the whole atmosphere, even though they can use a separate model for the boundary layer. They can also include calibration parameters based on empirical measurements at the location of interest.

In recent works, numerical models solving for the TKE have been used, e.g. in Meso-Nh[18,37] or with WRF.[20,38,39] Theoretical models based on Tatarskii's equations are also commonly used.[11,15,40] Finally, empirical models are also sometimes considered, such as the Trinquet-Vernin model.[41,42]

In this study, the C_n^2 model, Astro-Meso-Nh, presented in Ref. 18 has been chosen, namely because it is parametric and has already been used extensively in OT prediction for astronomy.[18,37] It relies on the TKE that is directly extracted from NWP simulations. As for several C_n^2 models, it is based on Gladstone's relationship[33] linking the refractive index structure parameter C_n^2 to the temperature structure parameter C_T^2:

$$C_n^2 = \left(\frac{80 \times 10^{-6}\, p}{T^2}\right)^2 C_T^2, \tag{2}$$

where p is the pressure in hectopascal and T is the temperature in kelvin. Equation (2) is obtained for a wavelength of 500 nm and is assumed to be valid for all visible wavelengths.[7] Different expressions for C_T^2 exist but they are usually derived from the Tatarskii's expression giving C_T^2 as the product between $L_0^{4/3}$ and the square of the temperature vertical gradient.[2] In Masciadri,[18] the chosen C_T^2 model is

$$C_T^2 = 0.58 \phi_3 L^{4/3} \left(\frac{\partial \bar{\theta}}{\partial z}\right)^2, \tag{3}$$

with $\bar{\theta}$ the grid-averaged value of the potential temperature.[13] In stable layers, the parameter ϕ_3 is equal to 0.78 and the mixing length L is the Deardoff length,[43] i.e.

$$L = \sqrt{\frac{2e}{\frac{g}{\theta_v}\frac{\partial \theta_v}{\partial z}}}, \tag{4}$$

where e is the TKE, g is the gravity of Earth and θ_v is the virtual potential temperature[44] obtained from $\theta_v = \theta\,(1 + 0.61r)$ for unsaturated air with mixing ratio r of water vapor.

Hence, this C_n^2 model involves macroscale meteorological quantities (pressure p, temperature T, potential temperature θ and mixing ratio r) that are directly obtained from WRF simulations. Computing the mixing length also requires the turbulent kinetic energy e that is thus added to the outputs of WRF. A similar C_n^2 model is used in Ref. 38, also relying on the C_T^2 Tatarskii's expression and a TKE model for the mixing length (assumed to be the outer scale L_0 in their work).

Figure 2 illustrates the contribution of the different factors in Eqs. (2) and (3) for Redu at 21:00 UTC on February 14, 2019. Turbulent layers, i.e. large values in the C_n^2 profile of Fig. 2f, are associated with large potential temperature gradient values (Fig. 2c) or large mixing length values (Fig. 2d). As seen in Fig. 2b, turbulent layers are associated with peak values of TKE. The TKE has a minimum value of 5×10^{-5} m^{2}s^{-2} set by default in WRF. A possible calibration of this minimum value based on C_n^2 profile measurements has already been presented in previous work[36] but was not applied in this study.

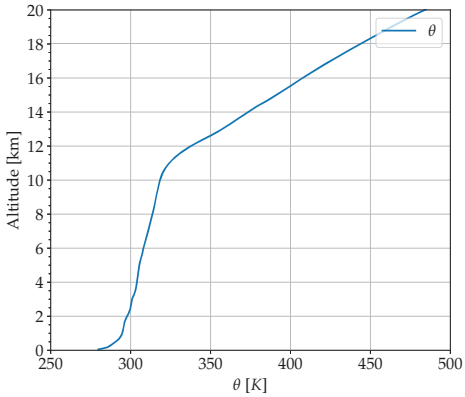

(a) Potential temperature

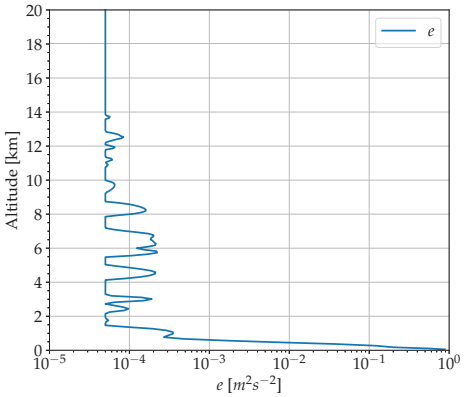

(b) TKE

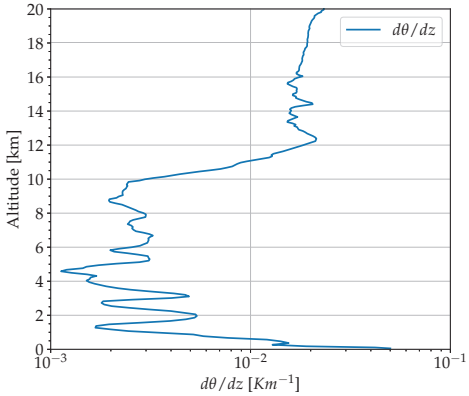

(c) Gradient of potential temperature

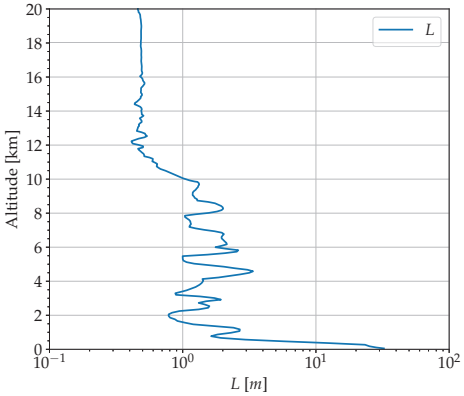

(d) Mixing length

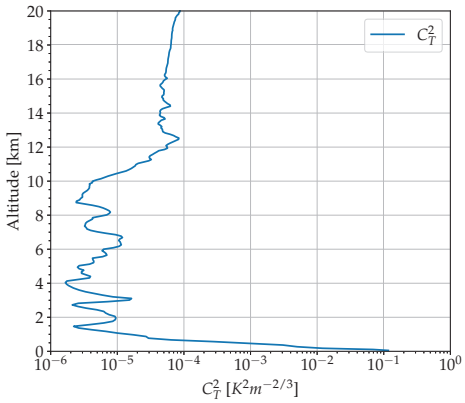

(e) Temperature structure parameter

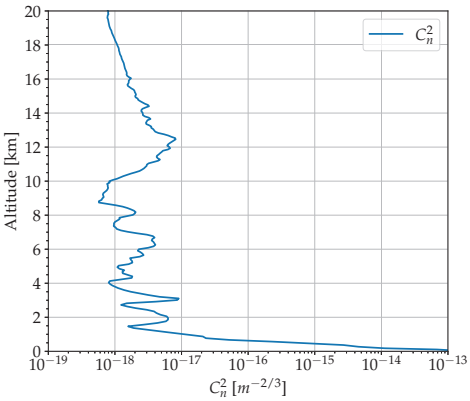

(f) Refractive index structure parameter

Figure 2: Illustration of the different factors involved in C_n^2 model for Redu at 21:00 UTC on February 14, 2019.

3.3 Boundary layer effects

The boundary layer is the portion of Earth's atmosphere close to the ground where effects coming from the Earth's surface are not negligible. Usually, turbulence is quite strong in this layer and is difficult to model. This is particularly a challenge at optical communication sites that are not located at high altitude and that suffer thus from stronger turbulence due to the boundary layer. A possible solution to ease this challenge is the use of hybrid C_n^2 models separating the free atmosphere from the surface layer.[45]

However, in this study, a single C_n^2 model for describing the whole atmosphere is preferred. It is made possible thanks to the use of the TKE that can also provide C_n^2 predictions in the boundary layer.

3.4 Availability of measurements

In order to validate the prediction capabilities of the model, measurements of C_n^2 profiles are not always available and integrated quantities (e.g. seeing, isoplanatic angle, scintillation index, etc.) are often much simpler to obtain. Nevertheless, as previously stated in Sec. 2, knowledge of C_n^2 profiles enables to obtain any integrated quantity of these profiles thanks to analytical expressions.

In the following section, seeing measurements at Redu will be compared to their predictions from NWP simulations. The seeing, noted ϵ_0, corresponds the full width at half maximum of the point spread function obtained when imaging through turbulence. It should be as small as possible and can be used to identify temporal windows during which the AO system will be most effective.[25] It is related to the Fried parameter r_0 by $\epsilon_0 = 0.98\lambda/r_0$, and is an integrated quantity of the C_n^2 profile that is often dominated by the surface layer.[46] Its analytical expression in the case of plane waves is given by

$$\epsilon_0 = 5.285\lambda^{-1/5} \left(\sec(\xi) \int_{h_0}^{\infty} C_n^2(h)\, \mathrm{d}h \right)^{3/5}, \tag{5}$$

where h_0 is the starting altitude (above ground) for the integration of the C_n^2 profile and ξ is the elevation angle measured from zenith, assumed to be 0° in the following. Hence, predictions of seeing come from Eq. (5) where simulated C_n^2 profiles have been integrated. They can then be compared to seeing measurements, obtained in this study using a differential image motion monitor (DIMM).[47]

A DIMM is a standard and widely spread instrument for seeing measurement. It can be easily implemented on a small amateur telescope, and uses typically a mask dividing the telescope pupil in two smaller subapertures. The seeing, or Fried parameter, is then estimated from the variance of the differential image motion of the two resulting spots (assuming one observes a star).[47] In the framework of SALTO,[17] a DIMM instrument has been set up using a Celestron C14 ($D = 35.6$ cm) with a mask of aperture size of $d = 12$ cm and a baseline of $B = 25$ cm. The DIMM software has been implemented following the prescriptions of Ref. 47. An illustration of the setup at Redu is given in Fig. 3.

4. APPLICATION TO SEEING PREDICTIONS AT REDU (BELGIUM)

The approach presented in Sec. 2 and parameterized in Sec. 3 has been validated with seeing measurements taken at Redu Space Services (ESA station) during the year 2019. Redu is located in the South of Belgium (50°00′06"N, 5°08′46.5"E) at an altitude of about 350 meters. Thanks to its ease of access, it is a potential candidate for future optical ground terminals in Belgium. It is therefore of major interest to study optical turbulence at this location. However, because of the relatively low altitude, important OT effects are expected from the boundary layer. This predominance of the boundary layer in the C_n^2 profile has already been observed in Fig. 2f, from 0 to $\sim$ 1.5 km of altitude above Redu, and is expected to lead to larger seeing values than at astronomical sites.

(a) DIMM setup at switch position.

(b) DIMM mask at the entrance of the telescope tube.

Figure 3: Illustration of the DIMM used at Redu in the framework of SALTO.

4.1 Results

Currently, three nights of measurements from the SALTO project are available (February 05, February 14 and September 04, 2019) and have been exploited for model validation.[17] Figure 4 depicts the evolution of measured and predicted seeing for February 14, 2019. DIMM measurements are available every 5 to 10 seconds and are relatively noisy (gray curve in the background of Fig. 4). A possible approach to deal with noisy measurements is filtering, this is the reason why a moving-average filter with a window of 50 points has been applied, leading to the orange curve. Alternatively, binning of the measurements in bins of 5 minutes has been performed. The average of all measurements falling in a given bin corresponds to the blue points, and the bars represent their standard deviation. Seeing predictions coming from WRF simulations with the TKE-based C_n^2 model correspond to the green squares, and are available every 5 minutes. Therefore, they can directly be compared with the average seeing value from the binned measurements. Finally, as a reference, seeing predictions coming from integration of the Hufnagel-Valley (HV) 5/7 profile are depicted in red.

WRF simulations have been performed with a lead time of 6 hours prior to the first available measurements. Computations of seeing from simulated C_n^2 profiles have been achieved using Eq. (5), starting the integration at an altitude h_0 of 100 meters up to 20 km. This starting altitude approximately corresponds to the first vertical level in WRF simulations and can be seen as a calibration parameter that is further discussed below.

As seen in Fig. 4, realistic seeing values are predicted by the model. However, they do not follow the short-term evolution of the measurements.

Comparison of seeing predictions and measurements for all three nights is depicted in Fig. 5. For every bin of 5 minutes where measurements are available, the measured average seeing is represented on the x-axis, whereas the y-axis shows the predicted seeing value for this 5-minute interval. For perfect seeing prediction, black points should fall on the dashed line. Moreover, the mean and standard deviation of the seeing measured and predicted for a complete night is depicted by the red points and bars.

Figure 5 shows that even though short-term predictions remain a challenge, long-term trends are similar: when the measured seeing is large for one night, the predicted seeing is also large. There is however an underestimation of the predicted seeing for one night (September 04, 2019), as seen from the cloud of points centered on the red point in (2.6;1). This underestimation results from a particularly low TKE value at the first WRF level, as well as a small gradient of potential temperature at this level.

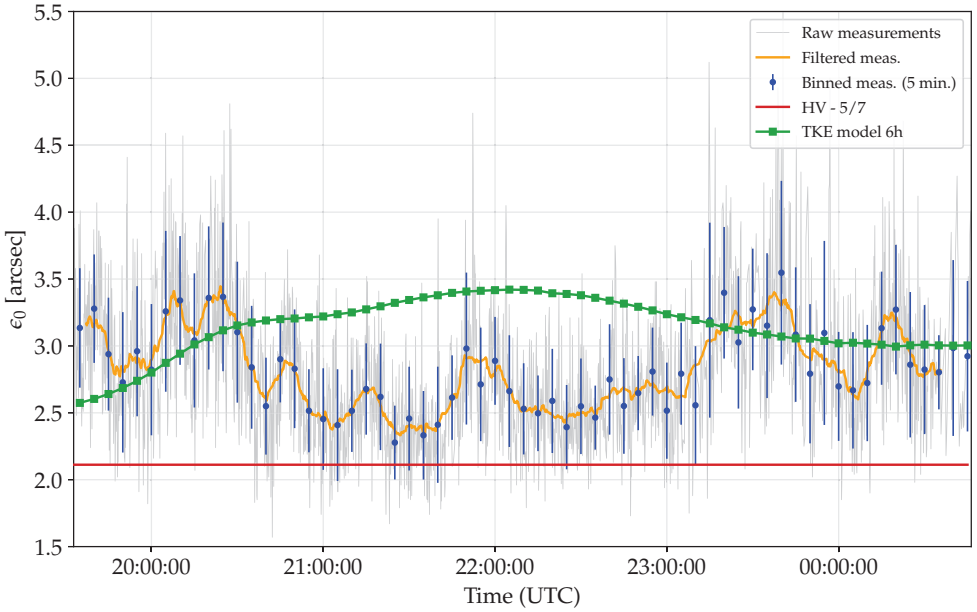

Figure 4: Prediction of seeing on February 14, 2019, at Redu (Belgium) and comparison with measurements.

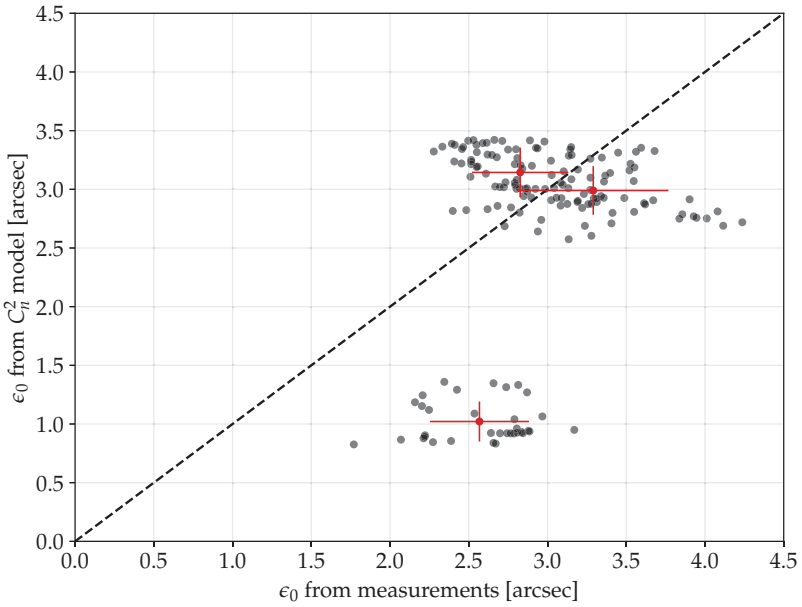

Figure 5: Correlation plot between measured seeing and predicted seeing for all three nights at Redu.

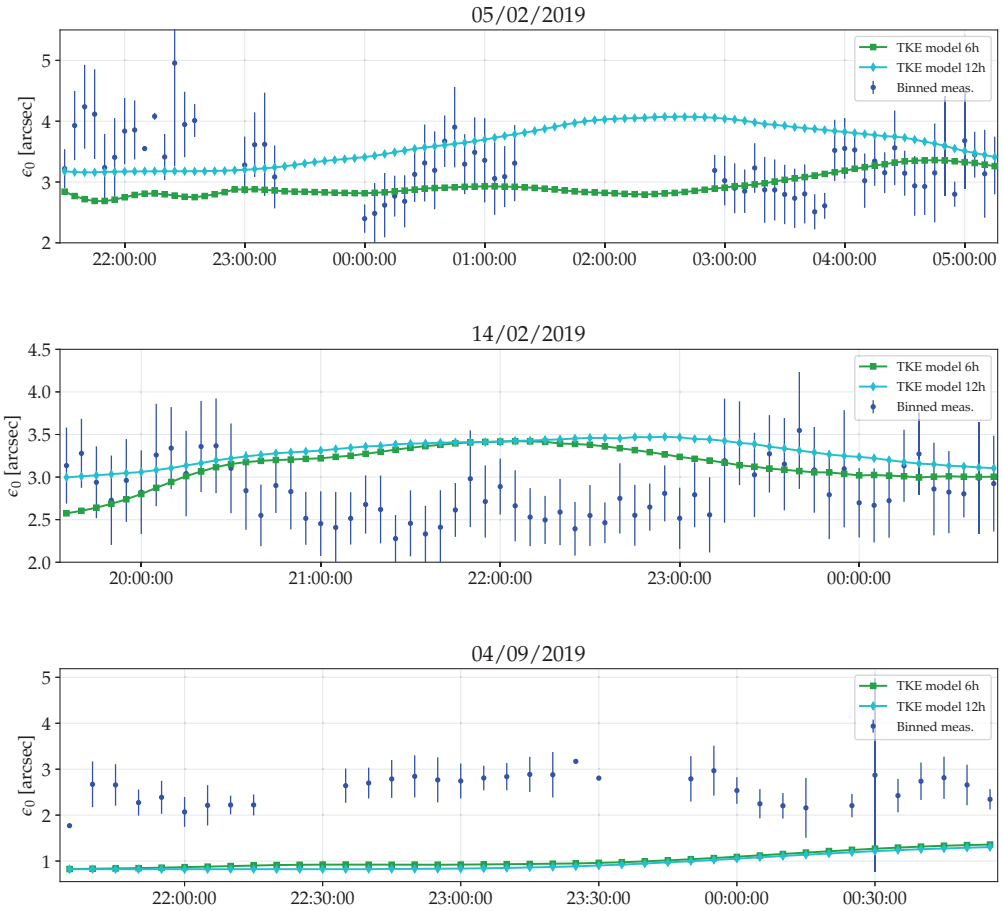

Figure 6: Seeing predictions for all three nights depending on the lead time (6 hours or 12 hours) in WRF simulations.

4.2 Discussion

Inaccuracies of (short-term) seeing predictions have been found to originate from limited prediction capabilities of NWP simulations as well as from the boundary layer C_n^2.

Prediction capabilities of NWPs Indeed, NWP models solve partial differential equations to obtain meteorological quantities on the desired grid and at given times. Since these equations are quite sensitive to the initial conditions (that are not known perfectly in practice), one can expect discrepancies between predictions and observations. Especially, the time at which a particular weather phenomenon is expected to happen is not always predicted properly, namely for phenomena with a small spatial extension and far in the future. Hence, when considering NWP models to study atmospheric impairments on electromagnetic wave propagation, comparisons are usually performed statistically.[48]

This effect is illustrated in Fig. 6 depicting the predicted seeing and the measurements for all three nights. The predictions come from the TKE-based C_n^2 model applied to NWP simulation outputs, with the only difference that the simulations are performed either with a lead time of 6 hours or a lead time of 12 hours. This variation of lead times introduces some changes in the meteorological quantities predicted during the night, hence impacting the predicted seeing at each instant. Nevertheless, average seeings over a given night remain consistent. A possible

Table 2: Average seeing and standard deviation per night, integration from h_0 to 500 m or 20 km of altitude.

Date	ϵ_0 from h_0 to 500 m	ϵ_0 from h_0 to 20 km
05/02/2019	$2.83'' \pm 0.35$	$2.99'' \pm 0.21$
14/02/2019	$3.11'' \pm 0.35$	$3.14'' \pm 0.21$
04/09/2019	$0.90'' \pm 0.19$	$1.02'' \pm 0.17$

solution to reduce such inaccuracies can be the use of mathematical models combining seeing observations and NWP predictions to provide accurate short-term seeing predictions. Such models have already been applied to astronomical sites.[14]

Boundary layer and seeing For seeing, accurate modelling of the boundary layer is paramount. As seen from Eq. (5), the integration only depends on the C_n^2 profile. Therefore, layers of large C_n^2 values tend to drastically impact the seeing. Since C_n^2 is usually the largest in the boundary layer, this layer dominates the seeing.[46]

As an example, Table 2 provides the average seeing for each night with different upper boundaries for the integral in Eq. (5). In both cases, integration starts from $h_0 = 100$ m but ends up either at 500 m or at 20 km. Results of Tab. 2 show that seeing at Redu arises mostly from the boundary layer, between h_0 to 500 m. Hence, if one is only interested in seeing predictions, there is no need to know the complete C_n^2 profile. Stated differently, it means that seeing measurements cannot be used solely to validate complete C_n^2 profiles. In order to overcome these limitations, other integrated quantities of C_n^2 profiles can be used. For example, the isoplanatic angle θ_0 involves a weighting function of the altitude in the integration, giving more importance to high-altitude C_n^2 values than to ground values.[15] Multi-aperture scintillation sensor (MASS) measurements can also provide free-atmosphere seeing, above the boundary layer.[39] Alternatively, measurements of C_n^2 profiles could be used to validate modelled C_n^2 profiles.

Moreover, extrapolating the C_n^2 value at 100 m (i.e. approximately from the first vertical level in WRF) up to the ground and starting the integration at $h_0 = 0$ m led to unrealistic seeing values, as large as 6 arcsec. This highlights the need for accurate descriptions of the boundary layer at optical communication sites where OT is largely dominated by this layer. It must be described with a spatial resolution larger than the one used in mesoscale simulations, either relying on hybrid C_n^2 models involving analytical profiles of C_n^2 in the boundary layer,[45] or using LES to increase the resolution at the price of a higher computational cost.

5. CONCLUSION

A general approach to perform optical turbulence characterization and prediction has been presented. It relies on NWP simulations and makes use of a C_n^2 model involving the turbulent kinetic energy.

Seeing measurements at Redu, Belgium, have been compared with seeing predictions for three different nights in 2019. The low availability of measurements was not sufficient to properly validate the approach. However, it highlighted the challenges of seeing prediction at optical communication sites. Since the boundary layer is expected to dominate optical turbulence at these sites, C_n^2 models offering accurate descriptions of this layer will be preferred. This motivates the use of C_n^2 models relying on the turbulent kinetic energy (as done in this paper) and the future development of hybrid models separating the free atmosphere from the boundary layer.

In the future, long-term measurements at Redu will help refining the model parameters and the description of the boundary layer. Approaches combining NWP simulation outputs with previous seeing measurements will be considered, especially for improving short-term seeing predictions. Long-term measurement campaigns at other optical communication sites are also encouraged in order to validate C_n^2 models suited for those sites and not for astronomical sites.

ACKNOWLEDGMENTS

The authors thank Redu Space Service for hosting and supporting the DIMM setup and related measurements. GOX, OAb, DVJ acknowledge the support from the Walloon region of Belgium through the program Skywin (project SALTO).

REFERENCES

[1] McKechnie, T. S., [*General theory of light propagation and imaging through the atmosphere*], Springer (2016).
[2] Tatarskii, V. I., "The effects of the turbulent atmosphere on wave propagation," *Jerusalem: Israel Program for Scientific Translations, 1971* (1971).
[3] Ishimaru, A., [*Wave propagation and scattering in random media*], vol. 2, Academic press New York (1978).
[4] Roddier, F., "V The effects of atmospheric turbulence in optical astronomy," in [*Progress in optics*], **19**, 281–376, Elsevier (1981).
[5] Hardy, J. W., [*Adaptive optics for astronomical telescopes*], vol. 16, Oxford University Press on Demand (1998).
[6] Ricklin, J. C., Hammel, S. M., Eaton, F. D., and Lachinova, S. L., "Atmospheric channel effects on free-space laser communication," *Journal of Optical and Fiber Communications Reports* **3**(2), 111–158 (2006).
[7] Andrews, L. C. and Phillips, R. L., [*Laser Beam Propagation through Random Media, Second Edition*], SPIE Press (2005).
[8] Osborn, J., Wilson, R., Sarazin, M., Butterley, T., Chacón, A., Derie, F., Farley, O., Haubois, X., Laidlaw, D., LeLouarn, M., et al., "Optical turbulence profiling with Stereo-SCIDAR for VLT and ELT," *Monthly Notices of the Royal Astronomical Society* **478**(1), 825–834 (2018).
[9] Haguenauer, P., Guesalaga, A., and Butterley, T., "Comparison of atmosphere profilers at Paranal and atmosphere parameters statistics: AOF-profiler, STEREO-SCIDAR, MASS-DIMM, LGS-WFS," in [*Adaptive Optics Systems VII*], **11448**, 345–359, SPIE (2020).
[10] Bi, C., Qian, X., Liu, Q., Zhu, W., Li, X., Luo, T., Wu, X., and Qing, C., "Estimating and measurement of atmospheric optical turbulence according to balloon-borne radiosonde for three sites in China," *JOSA A* **37**(11), 1785–1794 (2020).
[11] Qing, C., Wu, X., Li, X., Luo, T., Su, C., and Zhu, W., "Mesoscale optical turbulence simulations above Tibetan Plateau: first attempt," *Optics Express* **28**(4), 4571–4586 (2020).
[12] Coulman, C., Andre, J.-C., Lacarrere, P., and Gillingham, P., "The observation, calculation, and possible forecasting of astronomical seeing," *Publications of the Astronomical Society of the Pacific* **98**(601), 376 (1986).
[13] Bougeault, P., De Hui, C., Fleury, B., and Laurent, J., "Investigation of seeing by means of an atmospheric mesoscale numerical simulation," *Applied Optics* **34**(18), 3481–3488 (1995).
[14] Masciadri, E., Martelloni, G., and Turchi, A., "Filtering techniques to enhance optical turbulence forecast performances at short time-scales," *Monthly Notices of the Royal Astronomical Society* **492**(1), 140–152 (2020).
[15] Osborn, J. and Sarazin, M., "Atmospheric turbulence forecasting with a general circulation model for Cerro Paranal," *Monthly Notices of the Royal Astronomical Society* **480**(1), 1278–1299 (2018).
[16] CCSDS, G. B., "Real-time weather and atmospheric characterization data," *Informational Report, CCSDS* (2017).
[17] Orban de Xivry, G., Absil, O., Lismont, M., Moreau, V., Languy, F., and Vanhoenacker-Janvier, D., "Preliminary design of SALTO: the Belgian adaptive optics demonstrator," in [*Adaptive Optics Systems VI*], **10703**, 1070338, International Society for Optics and Photonics (2018).
[18] Masciadri, E., Vernin, J., and Bougeault, P., "3D mapping of optical turbulence using an atmospheric numerical model-I. a useful tool for the ground-based astronomy," *Astronomy and Astrophysics Supplement Series* **137**(1), 185–202 (1999).
[19] Cherubini, T., Businger, S., and Lyman, R., "Modeling optical turbulence and seeing over Mauna Kea: Verification and algorithm refinement," *Journal of Applied Meteorology and Climatology* **47**(12), 3033–3043 (2008).
[20] Basu, S., Osborn, J., He, P., and DeMarco, A., "Mesoscale modelling of optical turbulence in the atmosphere: the need for ultrahigh vertical grid resolution," *Monthly Notices of the Royal Astronomical Society* **497**(2), 2302–2308 (2020).
[21] Copernicus Climate Change Service (C3S), "ERA5: Fifth generation of ECMWF atmospheric reanalyses of the global climate," (2017). Copernicus Climate Change Service Climate Data Store (CDS), *Accessed 16 June 2021*, https://cds.climate.copernicus.eu/cdsapp#!/home.

[22] Skamarock, W. C., Klemp, J. B., Dudhia, J., Gill, D. O., Liu, Z., Berner, J., Huang, X. -yu., "A Description of the Advanced Research WRF Model Version 4," (2019). (No. NCAR/TN-556+STR). http://dx.doi.org/10.5065/1dfh-6p97.

[23] Qing, C., Wu, X., Li, X., Tian, Q., Liu, D., Rao, R., and Zhu, W., "Simulating the refractive index structure constant in the surface layer at Antarctica with a mesoscale model," *The Astronomical Journal* **155**(1), 37 (2017).

[24] Ullwer, C., Sprung, D., Sucher, E., Kociok, T., Grossmann, P., van Eijk, A. M., and Stein, K., "Global simulations of Cn2 using the Weather Research and Forecast Model WRF and comparison to experimental results," in [*Laser Communication and Propagation through the Atmosphere and Oceans VIII*], **11133**, 126–136, SPIE (2019).

[25] Masciadri, E., Lascaux, F., and Fini, L., "MOSE: operational forecast of the optical turbulence and atmospheric parameters at European Southern Observatory ground-based sites–I. Overview and vertical stratification of atmospheric parameters at 0–20 km," *Monthly Notices of the Royal Astronomical Society* **436**(3), 1968–1985 (2013).

[26] Hong, S.-Y. and Lim, J.-O. J., "The WRF single-moment 6-class microphysics scheme (WSM6)," *Asia-Pacific Journal of Atmospheric Sciences* **42**(2), 129–151 (2006).

[27] Zhang, C., Wang, Y., and Hamilton, K., "Improved representation of boundary layer clouds over the southeast Pacific in ARW-WRF using a modified Tiedtke cumulus parameterization scheme," *Monthly Weather Review* **139**(11), 3489–3513 (2011).

[28] Dudhia, J., "Numerical study of convection observed during the winter monsoon experiment using a mesoscale two-dimensional model," *Journal of Atmospheric Sciences* **46**(20), 3077–3107 (1989).

[29] Mlawer, E. J., Taubman, S. J., Brown, P. D., Iacono, M. J., and Clough, S. A., "Radiative transfer for inhomogeneous atmospheres: RRTM, a validated correlated-k model for the longwave," *Journal of Geophysical Research: Atmospheres* **102**(D14), 16663–16682 (1997).

[30] Jiménez, P. A., Dudhia, J., González-Rouco, J. F., Navarro, J., Montávez, J. P., and García-Bustamante, E., "A revised scheme for the WRF surface layer formulation," *Monthly Weather Review* **140**(3), 898–918 (2012).

[31] Nakanishi, M. and Niino, H., "Development of an improved turbulence closure model for the atmospheric boundary layer," *Journal of the Meteorological Society of Japan. Ser. II* **87**(5), 895–912 (2009).

[32] Good, R., Beland, R., Murphy, E., Brown, J., and Dewan, E., "Atmospheric models of optical turbulence," in [*Modeling of the Atmosphere*], **928**, 165–186, SPIE (1988).

[33] Beland, R. R., "Propagation through atmospheric optical turbulence," *Atmospheric Propagation of Radiation* **2**, 157–232 (1993).

[34] Andrews, L. C., Phillips, R. L., Wayne, D., Leclerc, T., Sauer, P., Crabbs, R., and Kiriazes, J., "Near-ground vertical profile of refractive-index fluctuations," in [*Atmospheric Propagation VI*], **7324**, 732402, International Society for Optics and Photonics (2009).

[35] Dewan, E. M., [*A Model for C2n (optical turbulence) profiles using radiosonde data*], no. 1121, Directorate of Geophysics, Air Force Materiel Command (1993).

[36] Hagelin, S., Masciadri, E., and Lascaux, F., "Optical turbulence simulations at Mt Graham using the Meso-NH model," *Monthly Notices of the Royal Astronomical Society* **412**(4), 2695–2706 (2011).

[37] Masciadri, E., Lascaux, F., Turchi, A., and Fini, L., "Optical turbulence forecast: ready for an operational application," *Monthly Notices of the Royal Astronomical Society* **466**(1), 520–539 (2017).

[38] Alliss, R. J. and Felton, B. D., "Numerical simulations of optical turbulence using an advanced atmospheric prediction model: Implications for adaptive optics design," in [*Proceedings of the Advanced Maui Optical and Space Surveillance Technologies Conference*], 9–12 (2014).

[39] Lyman, R., Cherubini, T., and Businger, S., "Forecasting seeing for the Maunakea Observatories," *Monthly Notices of the Royal Astronomical Society* **496**(4), 4734–4748 (2020).

[40] Rafalimanana, A., Giordano, C., Ziad, A., and Aristidi, E., "Prediction of atmospheric turbulence by means of WRF model for optical communications," in [*International Conference on Space Optics—ICSO 2020*], **11852**, 118524G, International Society for Optics and Photonics (2021).

[41] Trinquet, H. and Vernin, J., "A statistical model to forecast the profile of the index structure constant C_N^2," *Environmental Fluid Mechanics* **7**(5), 397–407 (2007).

[42] Giordano, C., Vernin, J., Trinquet, H., and Muñoz-Tuñón, C., "Weather Research and Forecasting prevision model as a tool to search for the best sites for astronomy: application to La Palma, Canary Islands," *Monthly Notices of the Royal Astronomical Society* **440**(3), 1964–1970 (2014).

[43] Deardorff, J. W., "Stratocumulus-capped mixed layers derived from a three-dimensional model," *Boundary-layer meteorology* **18**(4), 495–527 (1980).

[44] Stull, R. B., [*An introduction to boundary layer meteorology*], vol. 13, Springer Science & Business Media (1988).

[45] Vedrenne, N., Petit, C., Montmerle-Bonnefois, A., Lim, C., Conan, J.-M., Paillier, L., Velluet, M.-T., Caillault, K., Gustave, F., Durecu, A., et al., "Performance analysis of an adaptive optics based optical feeder link ground station," in [*International Conference on Space Optics—ICSO 2020*], **11852**, 527–535, SPIE (2021).

[46] Osborn, J., Föhring, D., Dhillon, V., and Wilson, R., "Atmospheric scintillation in astronomical photometry," *Monthly Notices of the Royal Astronomical Society* **452**(2), 1707–1716 (2015).

[47] Tokovinin, A., "From differential image motion to seeing," *Publications of the Astronomical Society of the Pacific* **114**(800), 1156 (2002).

[48] Quibus, L., "Modelling propagation impairments of Earth-Space links using Numerical Weather Prediction tools," *PhD thesis* (2020).